# The corrosion resistance and mechanism of AT13/Fe-based amorphous composite coatings

Zhenhua Chu[1*] , Shikun Teng[1],   Yuyun Zhou[1],   Xingwei Zheng[2**],   Jingxiang Xu[1],

Fang Wang[1], Baosen Zhang[3]

1. *Department of Mechanical Engineering, College of Engineering, Shanghai Ocean University, Shanghai, 201306, China*

2. *College of Science, Donghua University, shanghai, 201620, China*

3. *School of Materials Science and Technology, Nanjing Institute of Technology, Nanjing, 211167, China*

∗ Corresponding author:

 Zhenhua Chu    E-mail zhchu@shou.edu.cn    Tel: +86-22-60204810; Fax: +86-22-26564810

∗∗ Corresponding author:

Xingwei Zheng; E-mail zhengxingwei@dhu.edu.cn; Tel: +86-21-61900818; Fax: +86-21-61900

**Abstract:** In the present study, the corrosion resistance of amorphous coating and composite coatings in 3.5 wt.% NaCl, 0.5 M $H_2SO_4$ and 10 wt.% NaOH solution were studied. The composite coatings exhibit superior corrosion resistance. When the content of AT13 （$Al_2O_3$–13 wt.% $TiO_2$） was 15 wt.%, the composite coating has the lowest corrosion current density ($1.75 \times 10^{-6}$ A $cm^{-2}$), which is $5.14 \times 10^{-5}$ A $cm^{-2}$ for Fe-based metallic glassy coating, and the highest corrosion potential (-411 mV), which is -580 mV for Fe-based metallic glassy coating. The breakdown potential of the passivation film in 3.5 wt.% NaCl solution was much higher than that of 316L. The long-time immersion corrosion tests carried out on different coatings showed that the corrosion protection effect of coating was enhanced with the increase of the amount of AT13 added.


**Keywords:** Fe-based amorphous coating; AT13; Plasma spraying; Corrosion resistance

## 1.  Introduction

Although bulk metallic glasses (BMGs) exhibit ultrahigh hardness and strength, superior corrosion resistance and wear resistance [1-4], metallic glasses are seldom used in engineering, because of the limitation of the glassy formation ability. Fortunately, the metallic glassy coating can be fabricated by spraying method [5]. It is just need to put micron powders together then it can enlarge its size at 3-dimension. However, due to the deformation mechanism of bulk metallic glasses, which depends on the development of shear bands, it exhibits poor plastic deformation. As a result, a great amount of research efforts have been devoted to fabricate bulk metallic glassy composites (BMGCs) to improve the plasticity of BMGs by introducing ductile metallic crystalline or ceramic phases with high strength into the metallic glassy matrix in order to form multiple shear bands.

It is reported [6] that the amorphous composite coatings can improve the bonding and impact resistance of the coatings. Wang et al. [7] found that the WC phase-reinforced Fe-based amorphous coating is unstable in alkaline environment and then chemically reacts to dissolve, diminishing the corrosion resistance. Cai et al. [8] improved the wear resistance of the coating via enhancing the bonding strength between the ceramic particles and the matrix. In our previous studies [9-11], the excellent wear resistance and corrosion resistance were obtained in composite coatings. Electrochemical corrosion studies were made to further investigate the effect of the AT13(Al2O3–13 wt.% TiO2) ceramic phase on the fabricated materials in different aggressive media and the long-term corrosion mechanism. In the previous study [12], $ZrO_2$ ceramic powders were added

23  into the Fe-based metallic glassy coating by gas multiple-tunnel, due to high melting

24  temperature of $ZrO_2$. In this study, AT13 ceramic was adopted, due to lower melting

25  temperature, to fabricate composite Fe-based metallic glassy composite coating by

26  mixing Fe-based metallic powders and AT13 ceramic powders as feedback powders. It

27  is an easy method to obtain composite coatings. And it is worthy to note that the ability

28  of formation of amorphous isn't affected by addition of AT13.

29      In this paper, the coating corrosion resistance in different medium and the effect of

30  the second phase content on the electrochemical corrosion performance of the coatings

31  were studied. Moreover, the long-term corrosion behavior of amorphous composite

32  coating was evaluated in NaCl solution. It is observed that when the content of AT13

33  was 15 wt.%, the coating composite has the lowest corrosion current density and the

34  highest corrosion potential.

35  **2.  Experimental procedure**

36      $Fe_{54}Cr_{25}Mo_{17}C_2B_2$ alloy amorphous powders were produced by high pressure Ar gas

37  atomized. Then different weight fractions (5-20 %) of $Al_2O_3$–13 %$TiO_2$ (AT13) ceramic

38  powders (20-40 μm) were mixed with amorphous powders in a mechanical mixing

39  machine for 4 hours. The mild steel (0.45 wt.%C) was selected as substrate with a size

40  of 10 mm×10 mm×12 mm. All substrates were machined and polished, then degreased

41  by acetone, dried in air and grit-blasted prior the deposition. The coating was fabricated

42  by plasma spraying process.

43      The microstructures of powders and as-sprayed coating were examined by scanning

44  electron microscopy (SEM, S4800) coupled with energy dispersive spectroscopy (EDS)

45    and X-ray diffraction (XRD, Bruker D8 Focus).

46      Electrochemical measurements were performed at room temperature in a three-

47    electrode cell, therefore utilized the saturated calomel electrode (SCE) and the graphite

48    electrode as the reference and auxiliary electrode, respectively. Specimens for the

49    corrosion test were closely sealed with epoxy resin, leaving only an end-surface with a

50    surface area of $1*1$ cm$^2$ exposed for testing. The electrochemical behavior was

51    characterized by recording a Tafel plot at a potential sweep rate of 0.5 mVs$^{-1}$ from -100

52    mV to 1500 mV in 3.5 wt.% NaCl, 0.5M H$_2$SO$_4$ and 10 wt.% NaOH solution open to

53    air after immersing the specimens for an hour. Each test was repeated three times for

54    repeatability and reliability. In addition, electrochemical impedance spectroscopy (EIS)

55    was examined at OCP in 3.5 wt.% NaCl solution with sinusoidal amplitude of 10 mV

56    in the frequency ranging from $10^5$ Hz to 0.01 Hz. The impedance plots were interpreted

57    on the basic of the equivalent circuit using a suitable fitting procedure by Echem

58    Analyst. After EIS measurement, the corroded surface was examined by SEM.

59      For composition analysis in passivation film formed after electrochemical treatment,

60    a specimen was potentiodynamically polarized into the middle of the passive region

61    and then take out immediately for X-ray photoelectron spectroscopy.

62    **3.  Results**

63    3.1 Characterization of powders and as-sprayed coatings

64      The XRD spectra of mixed powders and amorphous composite coatings is shown in

65    Fig. 1. It can be seen that the mixed powders mainly contain Fe-based amorphous phase,

66    $\alpha$-Al$_2$O$_3$ phase and A-TiO$_2$ phase. With the increase of AT13 powder, the crystal peak

67    of $\alpha$-Al$_2$O$_3$ becomes more obvious, and the intensity value gradually increases. By

68    comparison, it is found that the $Al_2TiO_5$ crystal peak is observed more clearly when the

69    AT13 content in the composite powder increased to 20 % (Fig.1(a)). As is shown in Fig.

70    1(b), broad diffraction bump is appeared at the angle of $2\theta=43°\sim45°$ of all coatings.

71    Moreover, the crystal peak corresponding to the $\gamma$- $Al_2O_3$ phase also appeared in the

72    spectrum of the composite coatings, and the intensity of the diffraction peak increased

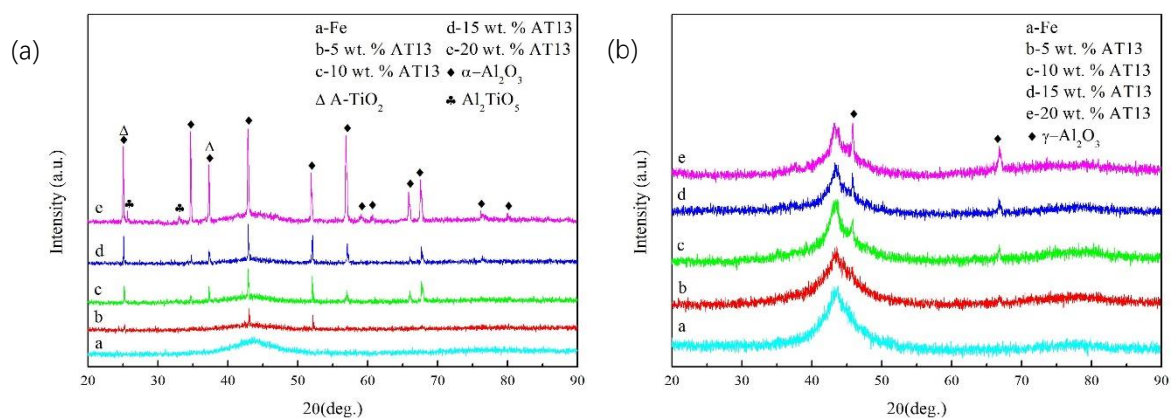73    with the increase of the content of the added content.

74
75
76
77
78
79
80



81    Fig. 1 (a) The XRD Spectra: (a) mixed powders; (b) amorphous composite
82                                    coatings

83    The surface morphology and structure of the cross-section of Fe-based amorphous

84    coating are shown in Fig. 2. It is found that as-sprayed coating is closely bonded to

85    substrate without obvious cracks. The amorphous coating exhibits a relatively uniform

86    and dense structure with a thickness of about 250 μm. In addition, the porosity of the

87    coating is about 4.305 %.

88
89
90
91
92
93

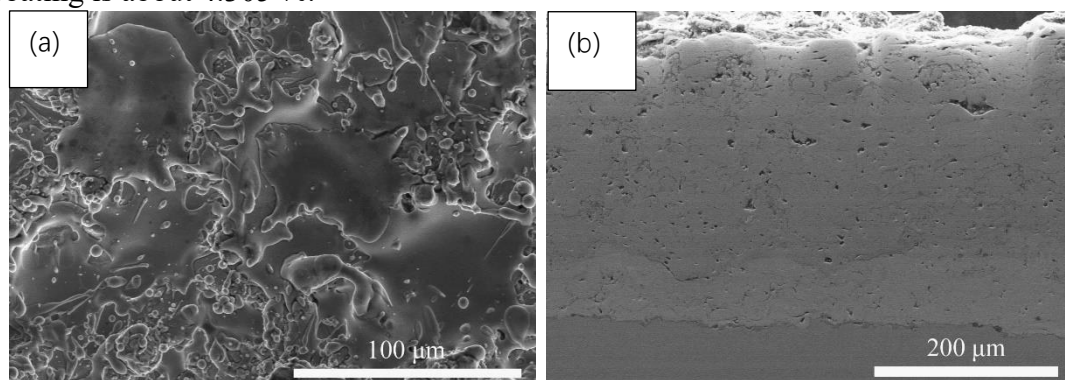94      Fig. 2 SEM images of (a) as-sprayed surface and (b) cross-section of amorphous

95                                                coating

96      3.2   Corrosion resistance measurements

97      3.2.1    Potentiodynamic polarization test

98      Fig. 3 displays the potendiodynamic polarization curves of different samples in

99      different corrosive solutions. Table 1 shows some electrochemical parameters, such as

100     corrosion potential ($E_{corr}$), corrosion current density ($i_{corr}$), transpassive current density

101     ($i_{pass}$), transpassive potential ($E_{tr}$) and corrosion rate. In 3.5 wt.% NaCl solution (Fig.

102     3(a)), the amorphous coating and composite coatings present excellent corrosion

103     resistance, and the self-corrosion potential is from -580 mV to -411 mV. Corrosion

104     current density on the order of $10^{-5}$ Acm$^2$~$10^{-6}$ Acm$^2$. The transpassive potential is up

105     to 1.0 $V_{SCE}$ and passivation region is more than 1.0 $V_{SCE}$. It reflected that there is an

106     effective passivation film on the surface, which can maintain stability in a wide range

107     and protect the matrix from corrosion. Moreover, with the addition of the AT13 ceramic

108     phase, the self-corrosion potential of the composite coatings was all positively shifted

109     compared with the pure Fe-based coating. The transpassive potential of 15 wt.% AT13

110     composite coating was up to 1.2 $V_{SCE}$, implying that the corrosion resistance of

111     composite coating is superior to the single amorphous coating. Comparing the self-

112     potential of 316L stainless steels with coatings, it was found that composite coating has

113     the best electrochemical parameters and the best corrosion resistance in a 3.5 wt.%

114     NaCl solution. In the 0.5M $H_2SO_4$ solutions (Fig. 3(b)), the curve of the self-corrosion

115     potential is very similar with the corrosion current indicating that the corrosion

116    resistance is not significantly different. Compared to the coating, 316L stainless steel

117    has higher self-corrosion potential and lower corrosion current, indicating little

118    corrosion tendency. In addition, the passivation current density of the 316L stainless

119    steel ($1.18 \times 10^{-5}$ A·cm$^{-2}$) is far lower than the coating ($1.98 \times 10^{-3}$ A·cm$^{-2}$), which

120    revealed that the corrosion resistance of 316L stainless steel in 0.5M $H_2SO_4$ solutions

121    is slightly better than the coating. Fig. 3(c) demonstrates the self-corrosion current

122    density of Fe-based amorphous coating and 316L stainless steel is low, but the

123    corresponding self-corrosion potential is -994 mV and - 418 mV, respectively.

124    Compared with 0.5M $H_2SO_4$ solution, the corrosion potential low about three times.

125    Besides, passivation film breakdown voltage is 0.5V and 0.2V. The results showed that

126    single coatings and 316L had higher corrosion tendency and worse local corrosion

127    resistance in NaOH solutions. It is more than that the self-corrosion potential and over-

128    passivation potential of amorphous coating are significantly lower than 316L. It

129    indicated that the corrosion resistance of amorphous coating is inferior to 316L in

130    NaOH solution. It can be also seen that with the addition of AT13 content, the current

131    density of the amorphous coating increases gradually, and other electrochemical

132    parameters decrease gradually. The range of activation increases, while the range of

133    stable passivation decreased slightly, indicating that the formation of passivation film

134    slowed down and the corrosion resistance weakened. Fe-based amorphous and

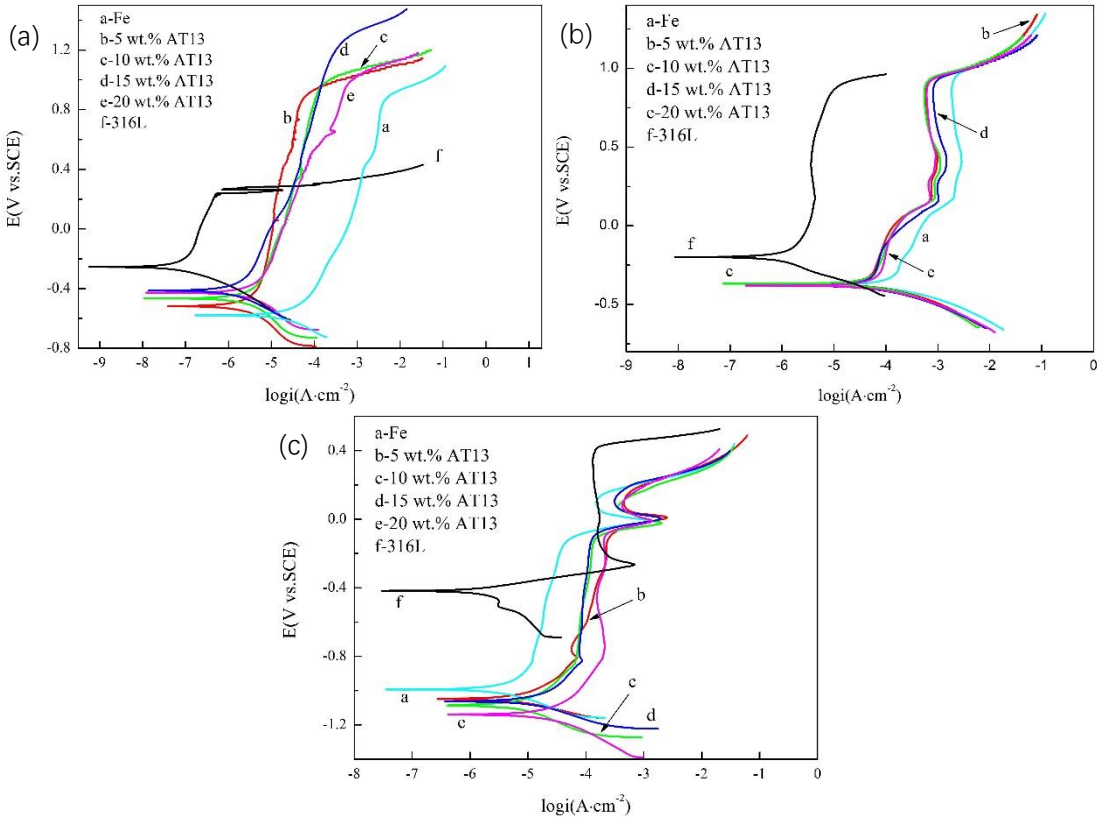135    composite coatings have better corrosion resistance in NaCl solution.

136

137

138

139      Fig. 3      Potentiodynamic polarization curves of different samples in

140   different corrosive solutions: (a) 3.5 wt.% NaCl; (b) 0.5 M $H_2SO_4$; (c) 10 wt.% NaOH

141            Table 1 Summary of the electrochemical parameters

| Corrosive medium | Coating | $E_{corr}$/mV | $i_{corr}$/A cm$^{-2}$ | $i_{pass}$/A cm$^{-2}$ | $E_{tr}$/mV | Corrosion rate/mpy |
|---|---|---|---|---|---|---|
| | Fe | -580 | $5.14 \times 10^{-5}$ | $5.42 \times 10^{-3}$ | 867 | 25.06 |
| | 5 wt.% AT13 | -519 | $7.50 \times 10^{-6}$ | $6.23 \times 10^{-5}$ | 905 | 6.47 |
| | 10 wt.% AT13 | -467 | $5.01 \times 10^{-6}$ | $1.12 \times 10^{-4}$ | 993 | 5.49 |
| 3.5%NaCl | 15 wt.% AT13 | -411 | $1.75 \times 10^{-6}$ | $5.37 \times 10^{-4}$ | 1236 | 2.07 |
| | 20 wt.% AT13 | -430 | $4.06 \times 10^{-6}$ | $6.94 \times 10^{-4}$ | 1012 | 4.60 |
| | 316L | -257 | $1.10 \times 10^{-7}$ | $8.07 \times 10^{-7}$ | 286 | 0.55 |

7

| | | | | | | |
|---|---|---|---|---|---|---|
| | Fe | -376 | $1.47\times10^{-4}$ | $1.98\times10^{-3}$ | 919 | 65.31 |
| | 5 wt.% AT13 | -368 | $6.29\times10^{-5}$ | $5.93\times10^{-4}$ | 904 | 57.81 |
| 0.5 M H$_2$SO$_4$ | 10 wt.% AT13 | -367 | $5.25\times10^{-5}$ | $6.24\times10^{-4}$ | 892 | 48.24 |
| | 15 wt.% AT13 | -380 | $6.51\times10^{-5}$ | $8.47\times10^{-4}$ | 896 | 59.80 |
| | 20 wt.% AT13 | -383 | $7.95\times10^{-5}$ | $6.52\times10^{-4}$ | 898 | 73.10 |
| | 316L | -199 | $4.24\times10^{-6}$ | $1.18\times10^{-5}$ | 877 | 3.90 |
| | Fe | -994 | $7.84\times10^{-6}$ | $5.46\times10^{-5}$ | -125 | 9.05 |
| | 5 wt.% AT13 | -1049 | $2.39\times10^{-5}$ | $2.46\times10^{-4}$ | -117 | 15.18 |
| 10%NaOH | 10 wt.% AT13 | -1096 | $1.68\times10^{-5}$ | $1.47\times10^{-4}$ | -102 | 15.40 |
| | 15 wt.% AT13 | -1063 | $2.38\times10^{-5}$ | $1.28\times10^{-4}$ | -98 | 21.89 |
| | 20 wt.% AT13 | -1145 | $4.40\times10^{-5}$ | $2.16\times10^{-4}$ | -96 | 40.45 |
| | 316L | -418 | $1.02\times10^{-6}$ | $1.48\times10^{-4}$ | 415 | 0.94 |

## 4. Analysis of corrosion morphology in different media

Fig. 4 depicts the surface corrosion morphologies of the amorphous coating, 15 wt.%AT13 composite coating and 316L after dynamic potential scanning to the over-passivation interval in NaCl solution. It is clearly seen that the severe corrosion of Fe-based amorphous coating in the spray pores and the edges of unmelted particles (Fig. 4a). Besides, amounts of evenly distributed corrosion holes appear on the surface (marked with white dotted circle). The results demonstrate that the coating mainly produces local pitting corrosion, the passivation film has failed, and the coating matrix dissolves rapidly. It can be seen that the corrosion of composite coating is obvious in holes and crevices, and the number of corrosion holes on the surface of the composite

152   coating is significantly less than that of pure coating (Fig. 4b), indicating that the

153   composite coating has stronger resistance to local corrosion than the pure amorphous

154   coating. The surface of the 316L stainless steel presents marked pitting corrosion hole

155   ($>60~\mu m$) (Fig. 4c). The size of that is much larger than the corrosion hole of the coating.

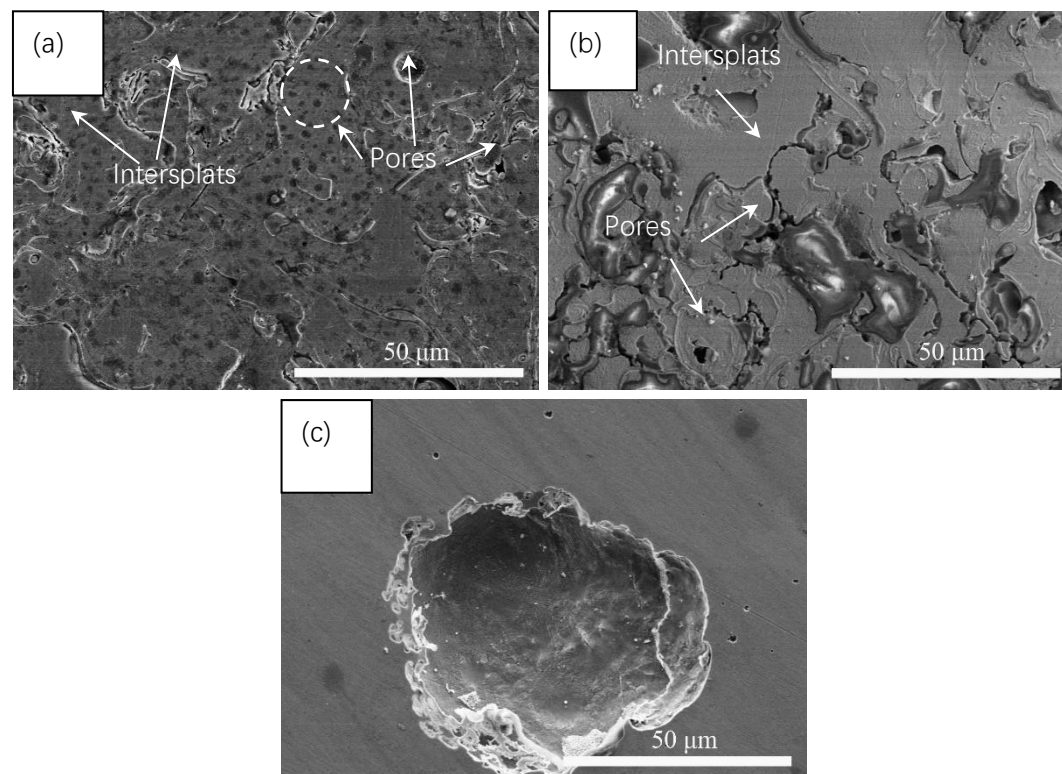156   Hence the local corrosion resistance of the 316L stainless steel is inferior than the

157   coating.

158



168   Fig. 4    SEM images of potentiodynamic polarization of different samples in 3.5wt.%

169    NaCl solution: (a) Fe-based amorphous coating; (b) 15 wt.%AT13 composite coating;

170                                    (c) 316L

171      The SEM images of the surface morphologies of the three samples after

172   potentiodynamic polarization in 0.5M $H_2SO_4$ solution are shown in Fig. 5. As seen in

173   Fig. 5a, amounts of pitting holes appear on the Fe-based amorphous coating surface.

9

174    Obviously, the size of pitting holes of the coating in 0.5M $H_2SO_4$ solution is much larger

175    than that of the coating in NaCl solution and crevice corrosion is more distinct with

176    accompanied by lamellar shedding. Compared with the pure coating, composite coating

177    remains the coating surface morphology (Fig. 5b), which means 316L stainless steel

178    has the best corrosion resistance in 0.5M $H_2SO_4$ solution and the corrosion resistance

179    of the composite coating is slightly better than of the single coating. Nevertheless, the

180    corrosion resistance of the coating in 0.5M $H_2SO_4$ solution is lower than that in 3.5 wt.%

181    NaCl solution. For 316L stainless steel, it has no obvious corrosion change, showing

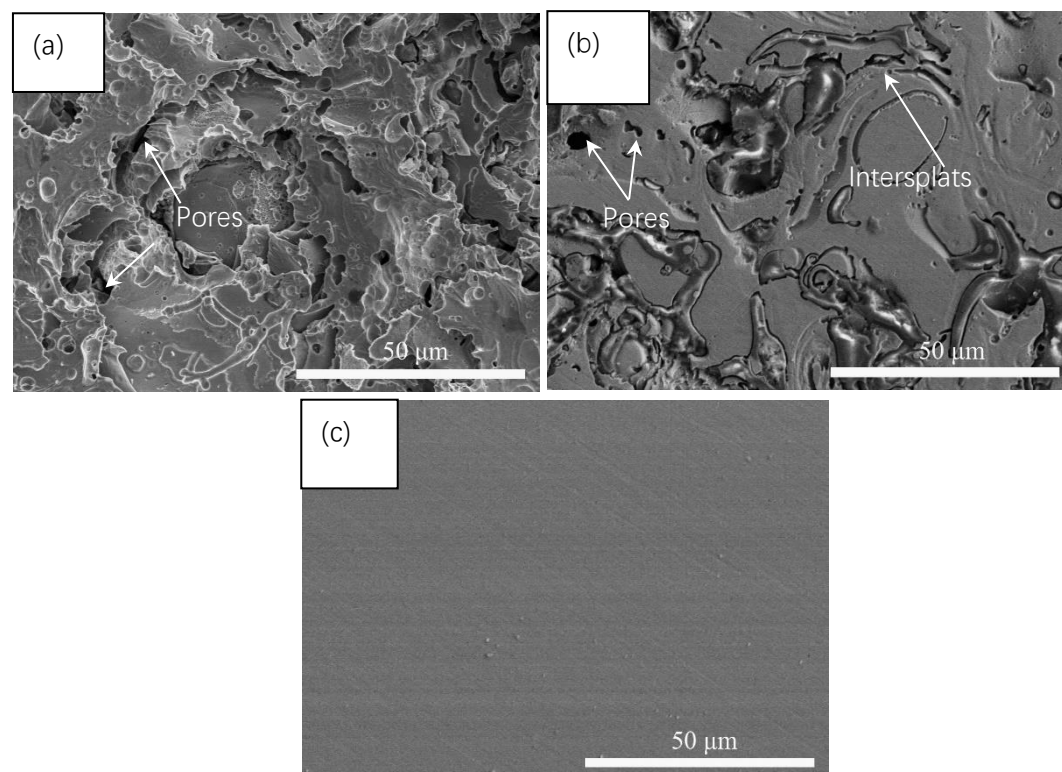182    excellent corrosion resistance (Fig. 5c).

183



193    Fig.5    SEM images of potentiodynamic polarization of different samples in 0.5 M

194          $H_2SO_4$ solution: (a) Fe-based amorphous coating; (b) 15 wt.%AT13 composite

195                    coating; (c) 316L

196 Fig. 6 presents the SEM images of potentiodynamic polarization of different samples

197 in 10 wt.% NaOH solution. A layer of reddish-brown corrosion product on the surface

198 of the Fe-based amorphous coating with a large number of lamellar shedding (Fig. 6a).

199 The reason of corrosion is mainly the sodium hydroxide solution penetrates the

200 interface between the coating and the substrate through the coating gaps and holes

201 during the dynamic potential scanning. Meanwhile, the coating dissolved rapidly and

202 the matrix reacts with the corrosion solution to produce a large amount of $Fe(OH)_2$ and

203 $Fe(OH)_3$. In comparison with single coating, composite coating surface is easier to peel

204 off (Fig. 6b), which is probably related to chemical relation. By further analysis, the

205 presence of $\gamma$-$Al_2O_3$ phase in the composite coating reacted with the NaOH solution

206 which accelerated the corrosion of coating. These observations reveal that with the

207 addition of AT13 ceramic phase, the corrosion resistance of Fe-based amorphous

208 coating obviously deteriorates in alkaline environment. Conversely, in the case of 316L

209 stainless steel, only a few micro-sized pitting holes are observed on the surface (Fig.

210 6c), showing the best corrosion resistance, which is consistent with result of the

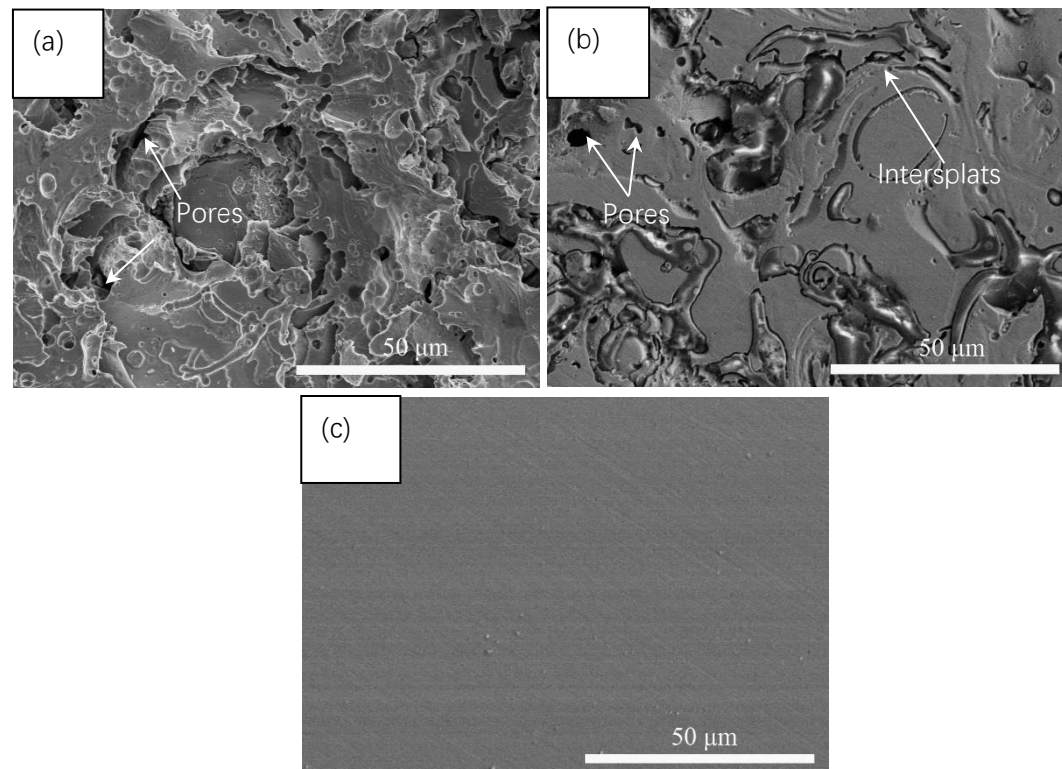211 polarization curve analysis.

212

213

214

215

216

217

218



Fig. 6 SEM images of potentiodynamic polarization of different samples in 10wt.%NaOH solution: (a) Fe-based amorphous coating; (b) 15 wt.%AT13 composite coating; (c) 316L

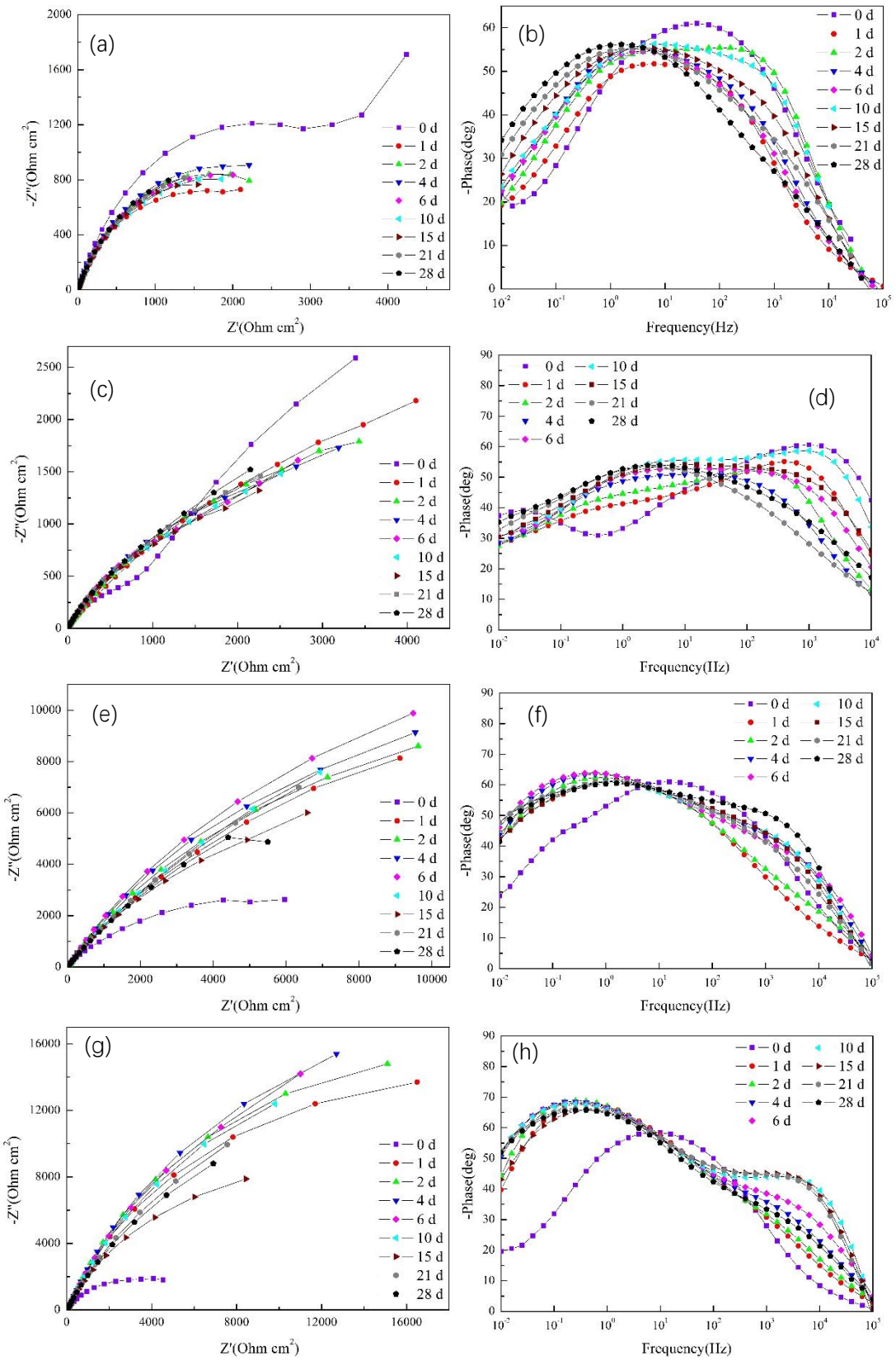## 5. Immersion test

5.1  EIS measurements

Potentiodynamic polarization and electrochemical impedance spectroscopy (EIS) measurements were performed to evaluate the corrosion resistance performances of coatings. The above experimental results show that the coating exhibit excellent corrosion resistance in 3.5 wt.% NaCl solution. In order to better evaluate the corrosion failure process of different coatings, long term immersion experiments in 3.5 wt.% NaCl solution combined with EIS measurements were carried out to analysis corrosion behavior of the coatings.

240    Fig. 7 illustrates the EIS plots of different coatings completely immersed in 3.5 wt.%

241    NaCl solution for 28 days. The Nyquist plots recorded at different period of immersion

242    time of the coatings are shown in Fig. 7a, c, e, g, i and panels b, d, f, h and j of Fig. 7

243    are the corresponding plots of phase angle versus logarithmic frequency. There exist

244    two stages of corrosion process of coatings: 0 d and 1 d-28 d. The data recorded at the

245    initial stage of corrosion exhibit two time constants due to relatively high porosity of

246    the coating. At the initial stage of immersion, Cl$^-$ ions present in solution has penetrated

247    into the coating from cracks and holes, and the galvanic corrosion reaction of the

248    chrome-poor and chrome-rich regions occurred near the interface between the unmelted

249    particles and layers to form a microcell [13].

250    For single coating, the impedance value is reduced from 1705 $\Omega \cdot cm^2$ to 731 $\Omega \cdot cm^2$.

251    And the impedance value of the 5 wt.% AT13 composite coating is reduced from 2587

252    $\Omega \cdot cm^2$ to 2160 $\Omega \cdot cm^2$. It is difficult to distinguish the two time constants due to the

253    capacitance arcs of the low frequency is not clear [14]. One time constant was in high

254    frequency range related to the capacitance impedance of the coating. The other constant

255    was in low frequency range related to charge transfer resistance and a double-layer

256    capacitance between the solution/coating interface. As immersion time increased, the

257    value of the resistance changed within a small range. During the 0day immersion, the

258    phase angle in the Bode phase plots (Fig. 7b and Fig. 7d) presents a maximum. With

259    the immersion increasing, the high frequency phase angle is shifted to left and the curve

260    drops, indicating more and more defects would be formed in coating due to corrosion.

261    In Fig. 7e, the Bode impedance plots of 10 wt.% AT13 composite coating shows two

262    continuous semi-circle shape. With the immersion increasing, the radius of capacitance

263    arc increased gradually, suggesting that the porosity of coating was further reduced and

264    the resistance of the passivation membrane to the electrolyte was enhanced. With the

265    immersion time to 10 day, the resistance value decreased gradually and then fluctuate

266    within a small range. The EIS plots of 15 wt.% and 20 wt.% AT13 composite coatings

267    in 3.5 wt.% NaCl solution for the 28 days are shown in Fig. 7g-j. There existed two

268    stages of the corrosion progress for the coatings: 0 day and after 1 day. At the 0 day, the

269    single capacitance resistance arc occurred in Bode impedance plots (shown in Fig. 7g

270    and Fig. 7i). It can be seen that the complete shielding layer was existed in the

271    composite coating, which prevented the corrosion effectively. The resistance value of

272    15 wt.% AT13 composite coating was 2780 $\Omega \cdot cm^2$ in the same time. Compared to 20

273    wt.% AT13 composite coating, the radius of semi-circle arc was bigger, indicating that

274    the corrosion resistance of 15 wt.% AT13 composite coating is better. After 1day

275    immersion, the Bode impedance plots showed two time constant, indicating that the

276    solution had reached oxide layer interface and the micro-galvanic reaction.

277    From the EIS plots of pure amorphous coating and composite coating, we can learn

278    that the radius of the capacitance resistance arc was the biggest when the addition of

279    AT13 is 15 wt.%, which suggested the corrosion resistance is improved. When

280    immersed for just 28 day, all coatings have not shown the characteristic Warburg

281    impedance caused by the diffusion of sodium chloride solution, indicating that the

282    coatings haven't yet lose the protective effect of the substance and have good corrosion
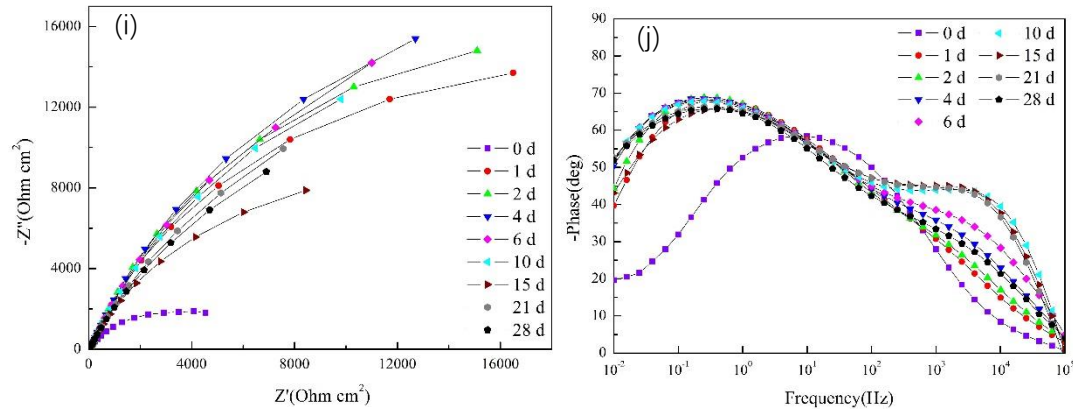
283    resistance.

14

Fig. 7 EIS plots of pure Fe-based coating,5 wt.%,10 wt.%,15 wt.% and 20 wt.%AT13

composite coatings cafter different immersion times:

(a)(c)(e)(g)(i) Nyquist plots; (b)(d)(f)(h)(j) Bode phase plot

The equivalent circuit model A (Fig. 8a) was used to simulate the EIS data at initial

stage corrosion of 15 wt.% and 20 wt.% AT13 composite coatings, which is composed

of the resistance of electrolyte solution (Rs), the CPE of coating ($Q_c$) in parallel with

the resistance of coating ($R_c$) and the CPE of double layer ($Q_{dl}$) in parallel with the

charge transfer resistance ($R_t$). Model B (Fig. 8b) was applied to the EIS data simulation

of Fe-based coating, 5 wt.%, 10 wt.% AT13 composite coatings and later stage

corrosion of 15 wt.% and 20 wt.% AT13 composite coatings. For model B, CPE-ct

represents a double-layer capacitance between oxide layer/coating interface. $R_{ct}$

represents charge transfer resistance.
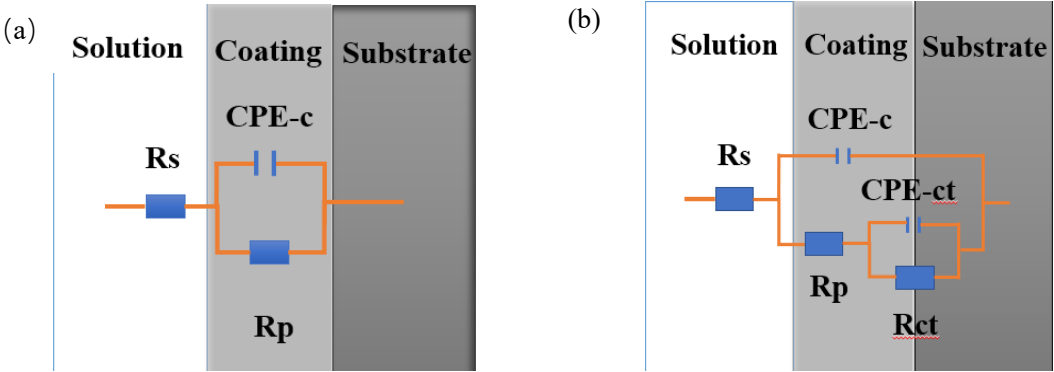
321  (a)

322

323

324

325

326

Fig. 8 The fitted equivalent circuits: (a) initial stage corrosion of 15 wt.% and 20 wt.%

AT13 composite coatings; (b) Fe-based coating, 5 wt.%, 10 wt.%AT13 composite

coatings and later stage corrosion of 15 wt.% and 20 wt.% AT13 composite coatings

The variation of electrochemical parameters for EIS spectra of coating with corrosion

time was shown in Fig. 9. At the initial stage, the maximum value of $R_p$ was $8.51 \times 10^3$

$\Omega \cdot cm^2$ (Fig. 9a), which implied that dense passivation produced in the coating surface

to prevent Cl$^-$ ion erosion. Compared to other coatings, the corrosion resistance of 15

wt.% AT13 composite coating is best. As the immersion time increased, the value of $R_p$

decreased sharply and then kept steady indicating that the corrosion products dissolved

into the solution gradually [15]. Fig. 9b showed the values of CPE-c increased

significantly when it increased to 21 day, suggesting that the protective ability of Fe-

based and 5 wt.% AT13 composite coatings greatly weakened due to the increase of

coating porosity. In Fig. 9c, we can see that the values of $R_{ct}$ increased correspondingly

with the addition of ceramic phase which indicated the composite coating enhanced a

hindrance to the corrosion solution. This proved that the corrosion resistance of 15 wt.%

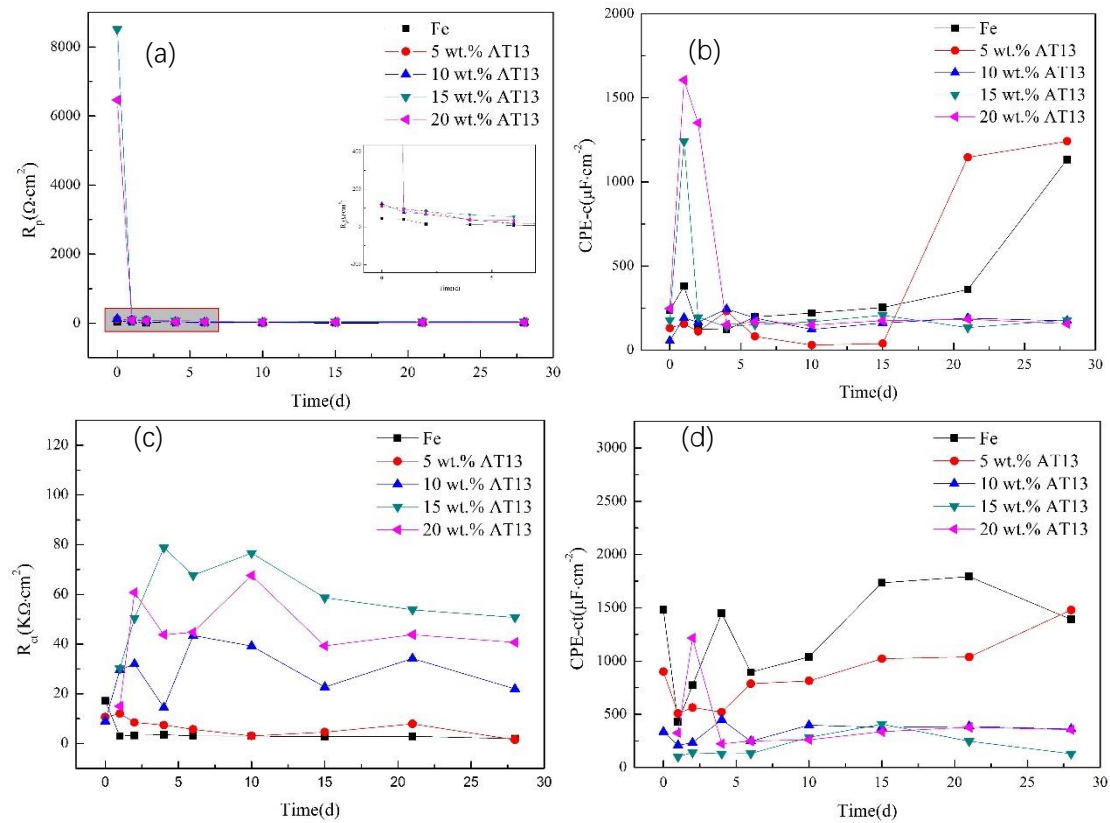AT13 composite coating is more superior to others, which is consistent with EIS result.

343

344

345

346

347

348

349

350

351

352

353



354     Fig. 9 The variation of electrochemical parameters for EIS spectra of coating with

355     corrosion time: (a) $R_p$-Time curve; (b) CPE-c-Time curve; (c) $R_{ct}$-Time curve; (d)

356     CPE-ct-Time curve

357     5.2   The analysis of surface element

358     In order to further analyze corrosion mechanism of different coatings, the Fe-based

359     amorphous coating and 15 wt.% AT13 composite coating were investigated by XPS.

360     Fig. 10 presented the XPS fine spectrum of Fe2p, Cr2p and Mo3d in the surface

361     passivation. As shown in Fig. 10a and Fig. 10b, the Fe2p$_{3/2}$ spectrum consists of

362     overlapped four peaks at 707 eV, 709~714 eV, which matches the $Fe^{2+}$ and $Fe^{3+}$

363     oxidation states[14]. In Fig. 10c and Fig. 10d, the Cr2p$_{3/2}$ spectrum can be resolved into

364     three peaks at 574 eV,576 eV and 578 eV. The peak at 574 eV, 576 eV and 578 eV

365  represent $Cr^0$ metallic state, $Cr^{3+}$ oxidation state and $Cr^{6+}$ oxidation state,

366  respectively[16]. Moreover, the $Co^0$ metallic state is just a part of $Cr2p_{3/2}$ spectrum. The

367  fitting results of the Mo3d spectrum were shown in Fig. 10e, f. Meanwhile, two peaks

368  at 228~229 eV and 230~231 eV were attributed to the $Mo^0$ metallic state. The peaks at

369  229~230 eV and 232~233 eV could be associated with $Mo^{3+}$ oxidation state. The peaks

370  at 233~234 eV and 234~236 eV were attributed to $Mo^{4+}$ oxidation state.

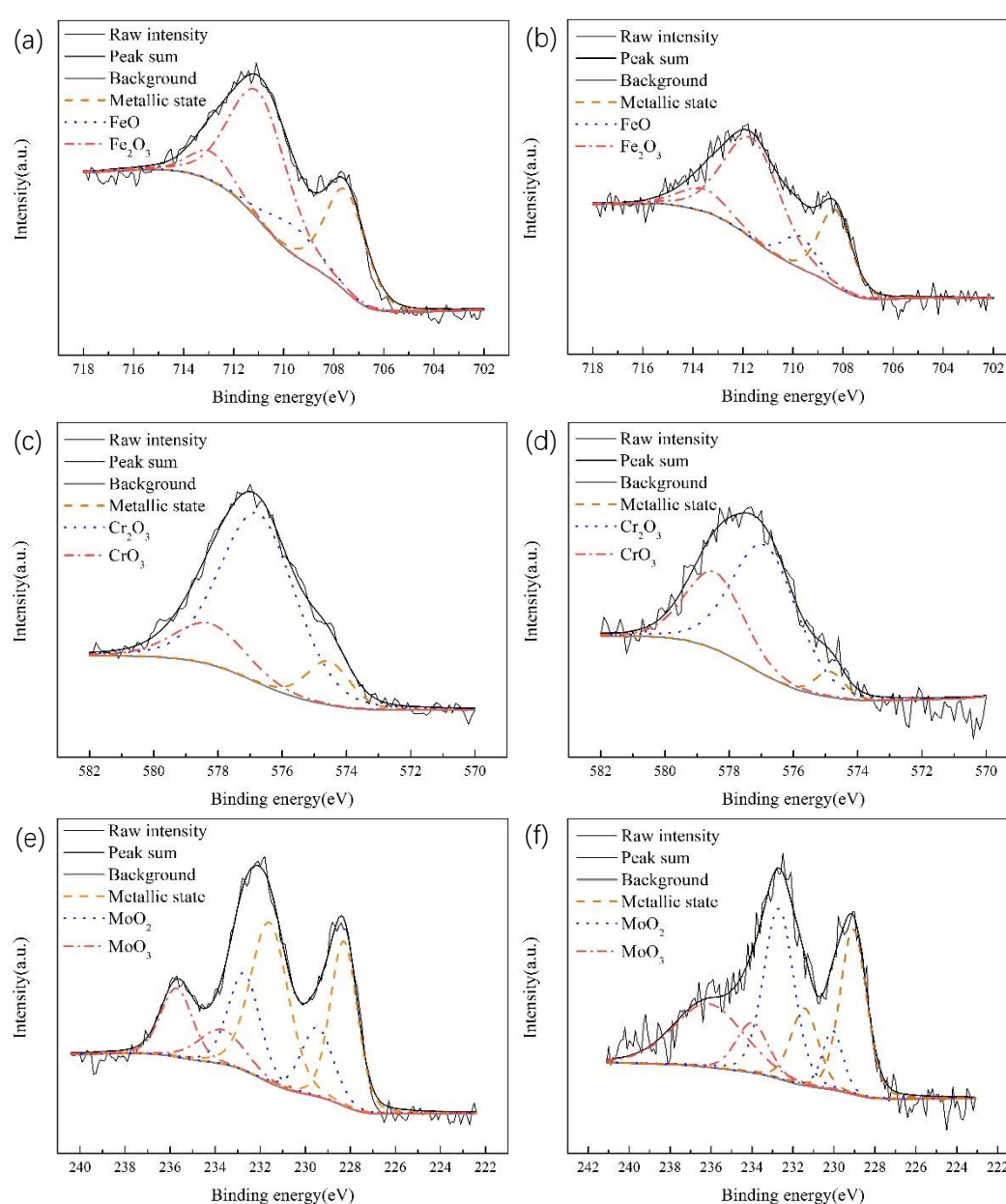

386  Fig. 10 XPS spectrum: (a)(c)(e) amorphous coating;

387                     (b)(d)(f)(g) 15 wt.%AT13 composite coating

388    The quantitative analysis of XPS results can be easily understand the corrosion

389    resistance mechanism of the coatings. We suppose that the metal ions in the oxidation

390    state are derived from the composition of the passivation film, and the metal ions

391    correspond to the passivation film/coating metal interface. The relative composition of

392    passivation film and the interface can be determined. Fig. 11 shows that cationic

393    component in the passivation film and atomic component at the coating interface. For

394    comparison, the passivation film of pure coating exhibited a higher Fe oxide content

395    and a lower Mo oxide content than the composite coating. In addition, the Mo3d

396    spectrum of the composite coating surface was mainly $Mo^{4+}$ oxide state. It was reported

397    [17] that $Mo^{4+}$ oxide in the passivation film can greatly improve the stability of

398    passivation film, thereby further enhance the local corrosion resistance. In this study,

399    the corrosion resistance of composite coating is better than that of the single coating.

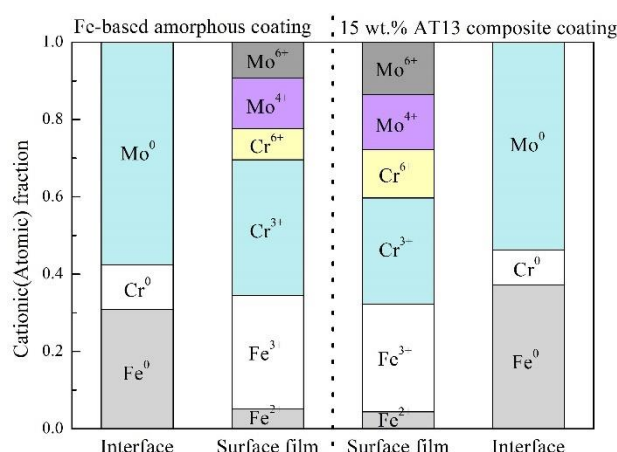400    This result is consistent with the EIS data mentioned above.

401



407    Fig. 11 Cationic fractions of the oxide species and atomic fractions of the metallic

408     species for the detected Fe, Cr and Mo elements by XPS from different coatings

409    5.3  The analysis of the corrosion morphology

410    To clarify the mechanism of the corrosion for the coatings, the surface corrosion

411    morphologies of the pure Fe-based coating and that of the 15 wt.% AT13 composite

412    coating after immersion for 28 days was investigated by SEM. As shown in Fig. 12, the

413    corrosion of coating surface was uneven. In addition, the corrosion preferentially

414    occurred at the edge of pore defect and the oxide [18]. Nevertheless, the corrosion of the

415    composite coating is less serious. This is because that many pores and micro-cracks

416    occurred in the single coating, and the Cr- rich and Cr-poor regions at the oxide edge

417    formed the micro-galvanic corrosion, which will become a preferential corrosion region,

418    leading to the ion penetration and corrosion reaction. As the corrosion time extends, the

419    coating peeled off and formed obvious pits. It indicates that the corrosion resistance of

420    coating is further deteriorated, but a large amount of corrosion products have not yet

421    accumulated.
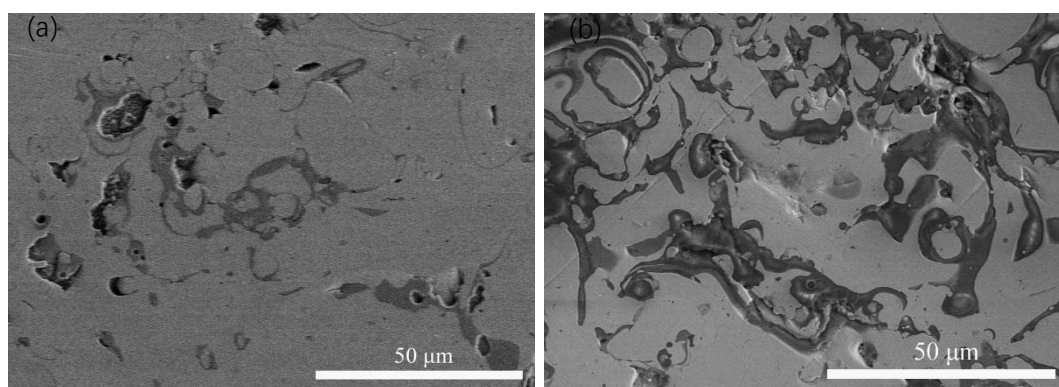
422



428    Fig. 12 Corrosion morphology after immersion in 3.5 wt.% NaCl solution for 28 days:

429              (a) pure Fe-based coating; (b) 15 wt.% AT13 composite coating

430

431    **6.   Research on long-term corrosion mechanism in NaCl solution**

432      The long-term corrosion mechanism diagram of composite coating is illustrated in

433    Fig. 13. As shown in Fig. 13a, there are some pore defects on the surface of the sample.

434    Meanwhile, there are mainly some interlayer gaps composed of oxide. Due to the flying

435    oxidation of particles during plasma spraying, Cr depleted areas are formed around the

436    pores [19]. However, when the coating was fully immersed, the pores on the surface will

437    be filled in NaCl solution. After that, the Cr depleted area around the pores will be

438    quickly dissolved (shown in Fig. 13b). Thus, a typical crevice corrosion reaction at the

439    micro-defects of the pores. At this time, the surrounding area will be further dissolved

440    because of the location advantage of the extreme occlusion in the hole and the harsh

441    corrosion environment. With the immersion time increases, the corrosion area of the

442    pores increases and the depth of the corrosion also increases. It gradually connected

443    with the internal closed pores and the intermediate layer, becoming a channel for

444    corrosion ions to invade the coating/substance interface (Fig. 13c). In general, with the

445    increase of AT13 content, the pore micro-defects and pore size in the composite coating

446    reduces. It is resulted that the probability and rate of the crevice corrosion reduces, and

447    the polarization test also shows lower corrosion current density and higher self-
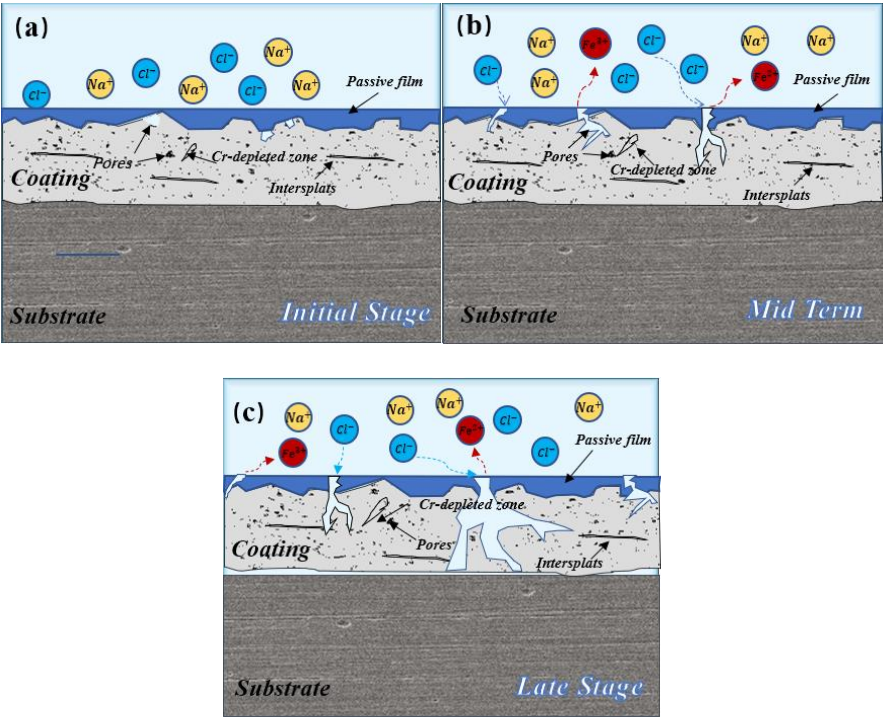
448    corrosion potential.

449



450

Fig. 13 The long-term corrosion mechanism diagram of composite coating: (a) initial

stages of corrosion; (b) mid stages of corrosion; (c) late stages of corrosion

**7.  Conclusion**

The coatings show the obvious passivation behavior in 3.5 wt.% NaCl solution,

and the breakdown potential of the passivation film (1.0 V) was much higher than that

of the 316L stainless steels (0.4 V). As the content of AT13 increase to 15wt.%, the

corrosion current density of coating reached the lowest and the self-corrosion potential

was the highest. It indicates that the addition of AT13 phase effectively improves the

corrosion resistance of the coating in simulated seawater.

Long term immersion corrosion was carried out on different coatings. The

impedance spectroscopy test results showed that the protective effect of the coating was

enhanced with the increase of the amount of the AT13. The equivalent circuit of pure

coating, 5 wt.% and 10 wt.% AT13 amorphous coating is R(Q(R(QR))). And the

464     equivalent circuit of the 15 wt.% and 20 wt.% AT13 amorphous coating increases

465     (R(QR)) to (R(Q(R(QR))).

## Acknowledgments

467     This work was supported by the National Nature Science Foundation of China

468     (No.51872072), The Excellent Youth Foundation of Jiangsu Scientific Committee

469     (grant number: BK20190103), Special funding for the development of science and

470     technology of Shanghai Ocean University (No. A2-0203-00-100231 and A2-2006-00-

471     200371).

## References

473     [1] H. Zhang, Y. Hu, G. Hou, Y. An, G. Liu, The effect of high-velocity oxy-fuel spraying parameters on
474     microstructure, corrosion and wear resistance of Fe-based metallic glass coatings. *Journal of Non-Crystalline Solids*
475     **406**, 37-44 (2014).
476     [2] H. S. Ni *et al.*, High performance amorphous steel coating prepared by HVOF thermal spraying. *Journal of Alloys
477     and Compounds* **467**, 163-167 (2009).
478     [3] W. H. Wang, C. Dong, C. H. Shek, Bulk metallic glasses. *Materials Science and Engineering: R: Reports* **44**, 45-
479     89 (2008).
480     [4] Y. Zhang *et al.*, Microstructures and properties of high-entropy alloys. *Progress in Materials Science* **61**, 1-93
481     (2014).
482     [5] C. Zhang *et al.*, Optimizing process and the properties of the sprayed Fe-based metallic glassy coating by plasma
483     spraying. *Surface and Coatings Technology* **319**, 1-5 (2017).
484     [6] M. Yasir, C. Zhang, W. Wang, Y. Jia, L. Liu, Enhancement of impact resistance of Fe-based amorphous coating
485     by Al2O3 dispersion. *Materials Letters* **171**, 112-116 (2016).
486     [7] S.-l. Wang, J.-c. Cheng, S.-H. Yi, L.-m. Ke, Corrosion resistance of Fe-based amorphous metallic matrix coating
487     fabricated by HVOF thermal spraying. *Transactions of Nonferrous Metals Society of China* **24**, 146-151 (2014).
488     [8] Y. Cai *et al.*, The effect of TiC/Al2O3 composite ceramic reinforcement on tribological behavior of laser cladding
489     Ni60 alloys coatings. *Surface and Coatings Technology* **291**, 222-229 (2016).
490     [9] Z. Chu *et al.*, Corrosion Mechanism of Plasma-Sprayed Fe-Based Amorphous Coatings with High Corrosion
491     Resistance. *Journal of Thermal Spray Technology* **29**, 1111-1118 (2020).
492     [10] Z. Chu, F. Wei, X. Zheng, C. Zhang, Y. Yang, Microstructure and properties of TiN/Fe-based amorphous
493     composite coatings fabricated by reactive plasma spraying. *Journal of Alloys and Compounds* **785**, 206-213 (2019).
494     [11] Z. Chu, X. Zheng, C. Zhang, J. Xu, L. Gao, Study the effect of AT13 addition on the properties of AT13/Fe-
495     based amorphous composite coatings. *Surface and Coatings Technology* **379**,   (2019).
496     [12] Z. Chu *et al.*, Characterization and tribology performance of Fe-based metallic glassy composite coatings
497     fabricated by gas multiple-tunnel plasma spraying. *Surface and Coatings Technology* **292**, 44-48 (2016).

[13] R. Q. Guo *et al.*, Study of structure and corrosion resistance of Fe-based amorphous coatings prepared by HVAF and HVOF. *Corrosion Science* **53**, 2351-2356 (2011).

[14] Y. Yang, C. Zhang, Y. Peng, Y. Yu, L. Liu, Effects of crystallization on the corrosion resistance of Fe-based amorphous coatings. *Corrosion Science* **59**, 10-19 (2012).

[15] J. M. Guilemany, J. Fernández, N. Espallargas, P. H. Suegama, A. V. Benedetti, Influence of spraying parameters on the electrochemical behaviour of HVOF thermally sprayed stainless steel coatings in 3.4% NaCl. *Surface and Coatings Technology* **200**, 3064-3072 (2006).

[16] J. C. Farmer *et al.*, Corrosion resistance of thermally sprayed high-boron iron-based amorphous-metal coatings: Fe49.7Cr18Mn1.9Mo7.4W1.6B15.2C3.8Si2.4 Cambridge University Press. **22**,    (2007).

[17] Y. Wang *et al.*, Electrochemical behaviour of Fe-based metallic glasses in acidic and neutral solutions. *Corrosion Science* **63**, 159-173 (2012).

[18] C. Zhang, K. C. Chan, Y. Wu, L. Liu, Pitting initiation in Fe-based amorphous coatings. *Acta Materialia* **60**, 4152-4159 (2012).

[19] J. Wu, S. D. Zhang, W. H. Sun, Y. Gao, J. Q. Wang, Enhanced corrosion resistance in Fe-based amorphous coatings through eliminating Cr-depleted zones. *Corrosion Science* **136**, 161-173 (2018).

## Captions List

Fig. 1 (a) The XRD Spectra: (a) mixed powders; (b) amorphous composite coatings

Fig. 2 SEM images of (a) as-sprayed surface and (b) cross-section of amorphous coating

Fig. 3 Potentiodynamic polarization curves of different samples in different corrosive

   solutions: (a) 3.5 wt.% NaCl; (b) 0.5 M H$_2$SO$_4$; (c) 10 wt.% NaOH

Table 1 Summary of the electrochemical parameters of each coating obtained from

   potentiodynamic polarization curves compared with 316L

Fig. 4 SEM images of potentiodynamic polarization of different samples in 3.5wt.%

   NaCl solution:

   (a) Fe-based amorphous coating; (b) 15 wt.%AT13 composite coating; (c) 316L

Fig. 5 SEM images of potentiodynamic polarization of different samples in 0.5 M

   H$_2$SO$_4$ solution: (a) Fe-based amorphous coating; (b) 15 wt.%AT13 composite

   coating; (c) 316L

Fig. 6 SEM images of potentiodynamic polarization of different samples in

527     10wt.%NaOH solution:(a) Fe-based amorphous coating; (b) 15 wt.%AT13

528     composite coating; (c) 316L

529  Fig. 7 EIS plots of pure Fe-based coating,5 wt.%,10 wt.%,15 wt.% and 20 wt.%AT13

530     composite coatings cafter different immersion times:(a)(c)(e)(g)(i) Nyquist plots;

531     (b)(d)(f)(h)(j) Bode phase plots

532  Fig. 8 The fitted equivalent circuits: (a) initial stage corrosion of 15 wt.% and 20 wt.%

533     AT13 composite coatings; (b) Fe-based coating, 5 wt.%, 10 wt.%AT13 composite

534     coatings and later stage corrosion of 15 wt.% and 20 wt.% AT13 composite

535     coatings

536  Fig. 9 The variation of electrochemical parameters for EIS spectra of coating with

537     corrosion time: (a) $R_p$-Time curve; (b) CPE-c-Time curve; (c) $R_{ct}$-Time curve; (d)

538     CPE-ct-Time curve

539  Fig. 10 XPS spectrum: (a)(c)(e) amorphous coating; (b)(d)(f)(g) 15 wt.%AT13

540     composite coating

541  Fig. 11 Cationic fractions of the oxide species and atomic fractions of the metallic

542     species for the detected Fe, Cr and Mo elements by XPS from different coatings

543  Fig. 12 Corrosion morphology after immersion in 3.5 wt.% NaCl solution for 28 days:

544     (a) pure Fe-based coating; (b) 15 wt.% AT13 composite coating

545  Fig. 13 The long-term corrosion mechanism diagram of pure Fe-based amorphous

546     coating and composite coating: (a)(b) schematic diagram of coatings; (c)(d)

547     initial stages of corrosion; (e)(f) late stages of corrosion